



OPEN

# Aqueous ionic effect on electrochemical breakdown of Si-dielectric–electrolyte interface

Jeongse Yun<sup>1,4</sup>, Jae Gyeong Lee<sup>1,4</sup>, Kyungbae Oh<sup>2</sup>, Kisuk Kang<sup>2,3</sup> & Taek Dong Chung<sup>1✉</sup>

The breakdown of thin dielectric films ( $\text{SiO}_2$ ,  $\text{Si}_3\text{N}_4$ ,  $\text{HfO}_2$ ) immersed in aqueous electrolyte was investigated. The current and the kinetics of dielectric breakdown caused by large cathodic electric field applied across the dielectric layer reveal the electrochemical nature of dielectric materials. Electrolytes play a huge role in the established dielectric–electrolyte interface with respect to the overall electrical behavior of the system. Although aqueous cations are considered as spectator ions in most electrochemical systems, in dielectric interfaces the current–potential characteristics depend on the type of cation. Computer simulation based on density functional theory and molecular dynamics showed cations affect the dielectric strength. The responses of various dielectric films to solution components provide invaluable information for dielectric-incorporated electrochemical systems.

The electrical conduction of inorganic insulating materials has been of keen and steady interest because it is critical for stability and reliability of electronic devices. Recently, the importance of insulators is rekindled due to its new found applications to batteries<sup>1–3</sup>, catalysts<sup>4–6</sup>, fundamental electrochemistry<sup>7</sup>, and iontronic devices<sup>8</sup>. The insulating thin film is more than an electrical and mechanical barrier protecting the underlying conductive material<sup>9</sup>. In electrochemical systems, it gives rise to certain characteristics that govern overall behavior, the reason for which is yet explored. For instance, unusual electrochemical phenomena is observed at  $\text{SiO}_2$ <sup>4,10,11</sup>, an extensively studied insulator.

Concerning the role of insulator as a material where the mass transport and electrochemical reactions of various species could take place, research hitherto has been focusing on mass transport and the redox process of cation species in the dielectric layer. Most of the literature concern hydrogen species and alkali metal ions such as sodium ion and potassium ion. There are many reports supporting that metal cations possibly transfer from solution to the insulating films such as  $\text{Si}_3\text{N}_4$ <sup>12,13</sup>,  $\text{HfO}_2$ <sup>14</sup> and  $\text{Al}_2\text{O}_3$ <sup>2,3,15,16</sup>. Particularly, proton involvement under the electrochemical reaction condition has been reported because they are expected to form quasi-stable states in the molecular chain of insulating materials. For example,  $\text{SiO}_2$  film becomes conductive after extensive contact with acidic solution for several hours<sup>10</sup>, but electric current hardly flows at as-prepared-dry  $\text{SiO}_2$  film<sup>17</sup>. Lee et al. showed electrochemical reactions mediated by hydrogen species within  $\text{SiO}_2$  thin films<sup>4,18</sup>.

Dielectric breakdown (DB) is the loss of electrical insulation under applied electric field. Current leaks through the dielectric layer when applied electric field and cleaves chemical bonds which lead to local disruption and loss of insulating property<sup>19</sup>. Its kinetics reflects the physical and chemical environment around the dielectric material. Therefore, DB can be indicative of the process of impregnation by cationic species. Briggs et al. studied how the pH of electrolyte affects the DB of  $\text{Si}_3\text{N}_4$ <sup>12</sup>. In addition to protons, various metal ions such as sodium and potassium ions were investigated with detailed physical and chemical models to characterize device failure<sup>20–23</sup>. It is believed that metal ions, which were impregnated during the fabrication process and the device operation, can move within the dielectric oxides. Yet how the metal ions travel within the dielectric layer and modify its properties is controversial. Impregnation of ions into the insulators mostly involves harsh conditions so that the intrinsic nature of insulator undergo severe changes far from its pristine state<sup>24–30</sup>, resulting in the inconsistency of experimental results. Therefore, the study on this type of system require a less invasive method that can minimally modify the property of as-deposited insulator film.

<sup>1</sup>Department of Chemistry, Seoul National University, Seoul 08826, Republic of Korea. <sup>2</sup>Department of Materials Science and Engineering, Research Institute for Advanced Materials (RIAM), Seoul National University, 1 Gwanak-ro, Gwanak-gu, Seoul 08826, Republic of Korea. <sup>3</sup>Institute of Engineering Research, College of Engineering, Seoul National University, 1 Gwanak-ro, Gwanak-gu, Seoul 08826, Republic of Korea. <sup>4</sup>These authors contributed equally: Jeongse Yun and Jae Gyeong Lee. ✉email: tdchung@snu.ac.kr

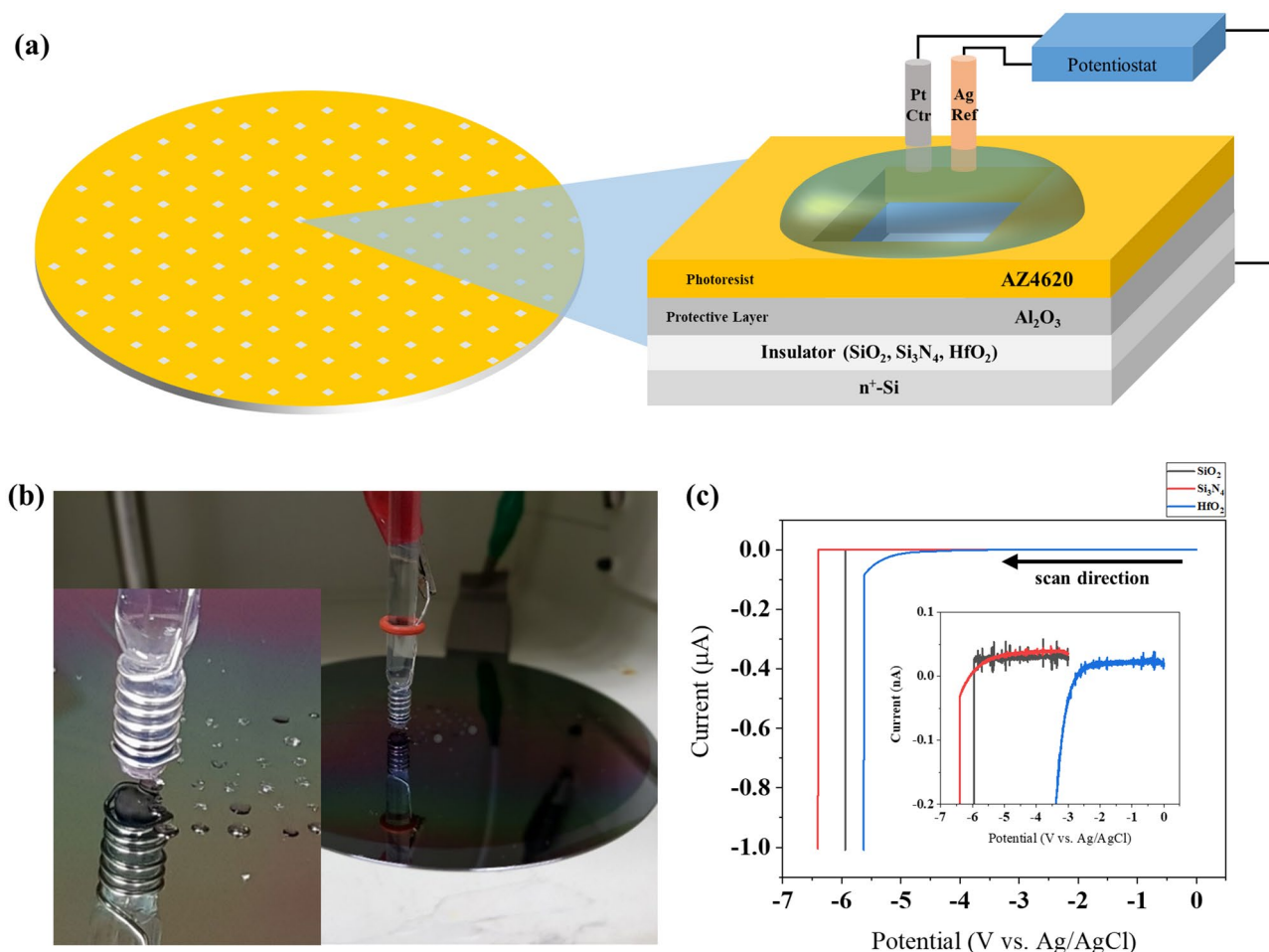


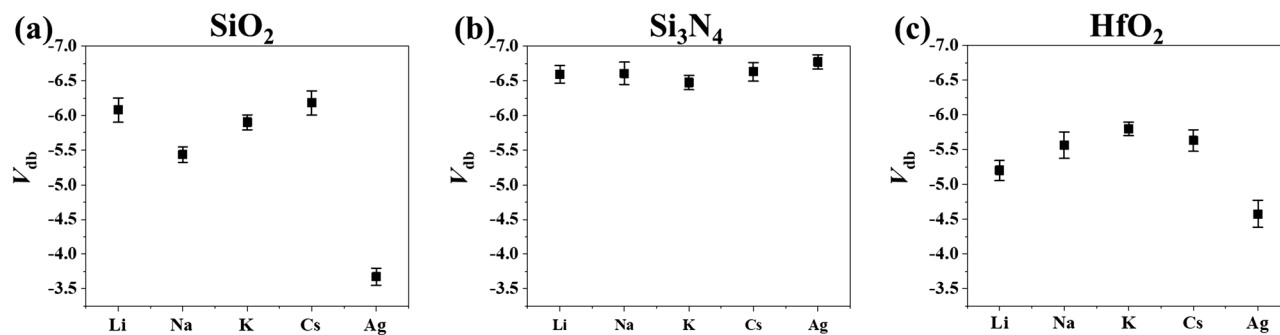
**Figure 1.** (a) Schematic diagram of electrochemical setup used in this study. Alumina and photoresist define the exposed area of insulators at  $50 \times 50 \mu\text{m}^2$ . Whole Silicon wafer serves as a working electrode to minimize unwanted physical damage during dicing or manual handling. Ctr is Pt wire counter electrode and Ref is Ag/AgCl (3 M KCl) reference electrode with a double junction filled with 1 M KNO<sub>3</sub>. (b) Image of the electrochemical cell. (c) Typical current–potential curve of Si-insulator (10 nm)-aqueous electrolyte system.

In this work, we investigated DB of commonly used dielectric films, SiO<sub>2</sub>, Si<sub>3</sub>N<sub>4</sub> and HfO<sub>2</sub> on a highly doped Si electrode, to which negative potential bias is applied. The electrochemical behavior and DB kinetics allows monitoring of the effect of metal ions on the electrolyte–oxide–semiconductor (EOS) system.

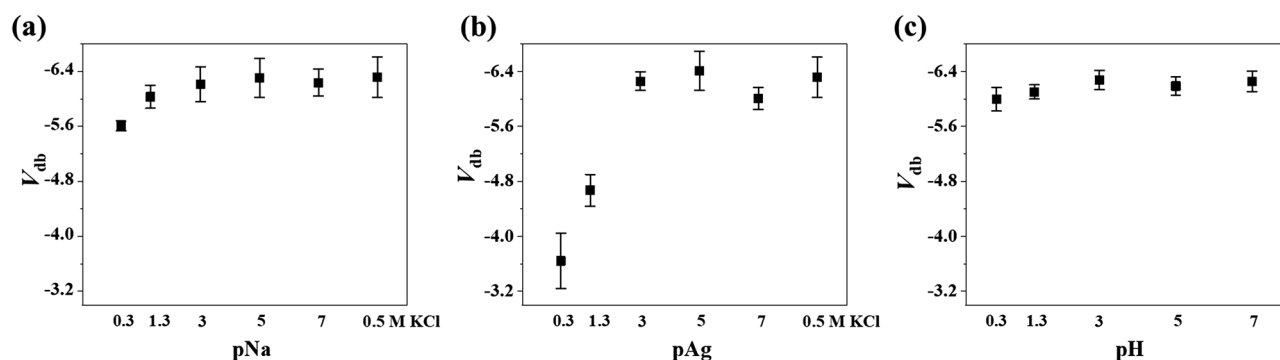
## Results and discussion

Figure 1a,b show the experimental setup of the three-electrode configuration connected to a potentiostat. Typical voltammograms of SiO<sub>2</sub>, Si<sub>3</sub>N<sub>4</sub> and HfO<sub>2</sub> deposited on Si obtained in 0.5 M KCl are presented in Fig. 1c. The current surge indicates dielectric breakdown (DB) of the thin insulating film. Indicated on the  $i$ - $V$  curves of SiO<sub>2</sub>, Si<sub>3</sub>N<sub>4</sub> and HfO<sub>2</sub> is the dielectric breakdown potential,  $V_{\text{db}}$ . Current starts to increase before  $V_{\text{db}}$  for Si<sub>3</sub>N<sub>4</sub> and HfO<sub>2</sub>, but for SiO<sub>2</sub> only a small charging current flows. Band gap for Si<sub>3</sub>N<sub>4</sub> and HfO<sub>2</sub> is 5.3 eV<sup>31</sup> and 5.7 eV<sup>32</sup>, respectively, which are much smaller than 9 eV for SiO<sub>2</sub>. This explains the current flow through the film under smaller bias at Si<sub>3</sub>N<sub>4</sub> and HfO<sub>2</sub>. Before the breakdown, the electric field where leakage current begins to flow is about 6 MV/cm, 2 MV/cm, and 1 MV/cm for SiO<sub>2</sub>, Si<sub>3</sub>N<sub>4</sub>, and HfO<sub>2</sub>, respectively<sup>33,34</sup>. Inset of Fig. 1c shows a similar trend, therefore the electrolyte is not responsible for the exponential leakage current that appears before DB. Leakage current before breakdown flows through HfO<sub>2</sub> unlike SiO<sub>2</sub> and Si<sub>3</sub>N<sub>4</sub>, which is supposedly related to defects such as oxygen vacancies<sup>35</sup>. The breakdown voltages of HfO<sub>2</sub> were taken where the current surges in Fig. 1c.

To investigate cationic effect on DB in EOS system, the  $i$ - $V$  curves were obtained in the presence of alkali metal ions (Li<sup>+</sup>, Na<sup>+</sup>, K<sup>+</sup>, Cs<sup>+</sup>) and silver ion (Ag<sup>+</sup>). The results from solutions containing NaCl and AgNO<sub>3</sub> are conspicuous in that  $V_{\text{db}}$  positively shifts for SiO<sub>2</sub> (Fig. 2a). Plasma-enhanced chemical vapor deposition (PECVD) SiO<sub>2</sub> also showed a similar  $V_{\text{db}}$  trend (Fig. S1), indicating that it is a feature shared by the SiO<sub>2</sub> material rather than the method for fabricating thin insulating film. This should be attributed to effects of sodium and silver cations because anionic effect is negligible (Fig. S2). The cationic effect on the breakdown is a function of concentration. Figure 3 shows that both sodium ion, silver ion, and proton have little influence on breakdown of SiO<sub>2</sub> at concentrations below 1 mM. Furthermore, silver ion causes  $V_{\text{db}}$  to shift to a much greater extent than



**Figure 2.** Potential at which dielectric breakdown occurs ( $V_{db}$ ) depending on metal cations in aqueous electrolyte. (a) Si– $\text{SiO}_2$  (10 nm)-electrolyte, (b) Si– $\text{Si}_3\text{N}_4$  (10 nm)-electrolyte, (c) Si– $\text{HfO}_2$  (10 nm)-electrolyte.



**Figure 3.** Potential at which dielectric breakdown occurs ( $V_{db}$ ) for  $\text{SiO}_2$  as a function of (a) sodium ion concentration, (b) silver ion concentration, and (c) proton concentration.

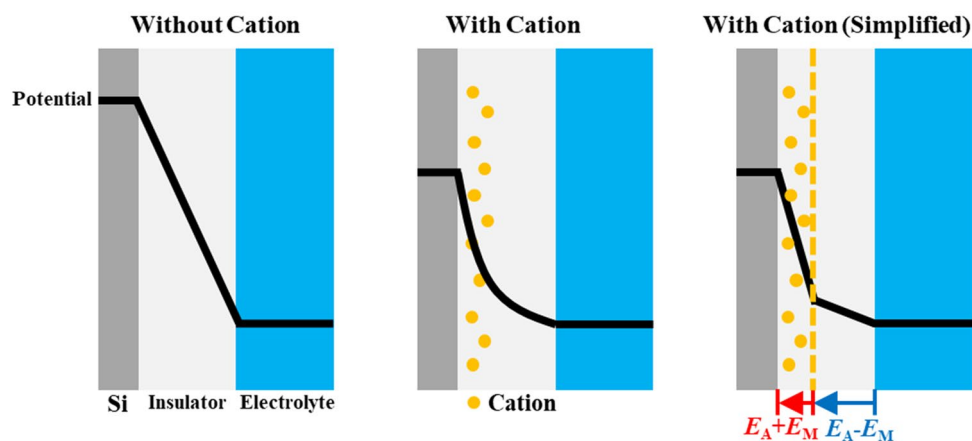


**Figure 4.** Potential diagrams of Si– $\text{SiO}_2$ -electrolyte systems with or without transferrable cations in electrolyte.

sodium ion,  $V_{db}$  being approximately 2.5 V and 0.7 V, respectively.  $V_{db}$  shift of proton is 0.25 V and more similar to sodium ion than silver ion. It is increasingly probable that  $\text{SiO}_2$  film undergoes breakdown at lower voltage, i.e. weaker electric field, in the presence of sodium ion, silver ion and proton at concentration higher than 1 mM.

Concerning the influence of sodium and silver ions on DB of  $\text{SiO}_2$ , there are a few reports that mobile cations that forcibly impregnated in dielectric films during the fabrication lower  $V_{db}$  increasingly with effective electric field (Fig. 4)<sup>20,21</sup>. In this system, metal ions are initially absent in the  $\text{SiO}_2$  film and present in the solution. Therefore, the cations should transfer from the aqueous phase to the  $\text{SiO}_2$  layer upon negative electric bias.

Based on the assumption that the transferred sodium and silver ions weaken the dielectric strength by modifying the effective electric field, we estimated the number of sodium and silver ions transferred into  $\text{SiO}_2$  by employing the methodology to analyze the introduction of cations to hydrogenated silicon carbon nitride film<sup>21</sup>. Briefly, we positioned sodium or silver ions on a plane and calculated the effective electric field by summation

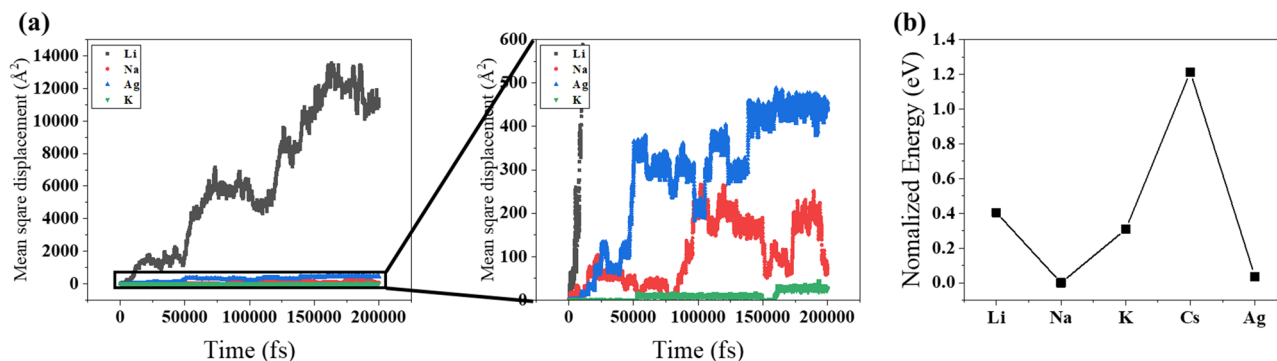


**Figure 5.** (a) Mean square displacement of cations versus time for different metal ions calculated by AIMD simulation. (b) Normalized free energy required for cation transport from aqueous to SiO<sub>2</sub> phase.

of the applied field and the field generated by the ions. Potential differences at the interfaces of Si–SiO<sub>2</sub> and SiO<sub>2</sub>–electrolyte are not considered because the applied voltage is significantly larger. Thus, the magnitude of applied field gradient,  $E_A$ , would be  $V_A/d$  where  $V_A$  is applied voltage between reference electrode and Si and  $d$  is the oxide thickness. By the Gauss law, electric field created by sodium ion on a plane in the film should have the magnitude of  $E_M = qN_M/2\epsilon$  where  $q$  is the charge of electron,  $N_M$  is area density of sodium or silver ion,  $\epsilon$  is the permittivity of free space. Thus, the electric field applied between Si and the plane of sodium or silver ion is  $E_{total} = E_A + E_M = V_A/d + qN_M/2\epsilon$ . When  $E_{total}$  exceeds the dielectric strength of SiO<sub>2</sub>, which is  $V_{db}/d$  in the absence of sodium and silver ions, breakdown should occur. Using the measured  $V_{db}$  in Fig. 2a, we estimated the number of ions per unit area of 10 nm-thick film,  $7.67 \times 10^{15} \text{ m}^{-2}$ , one sodium ion per 3000 SiO<sub>2</sub>, or 13 mM. In the same way, the estimated number of silver ions per unit area of 10 nm-thick film is  $2.94 \times 10^{16} \text{ m}^{-2}$ , one silver ion per 780 SiO<sub>2</sub>, or 49 mM.

As for transportation of cation between two different phases, we can divide its entire process into 3 steps. (1) The solvation shell of the cation in solution phase would be completely or partially removed before entering the oxide phase. (2) In the oxide, the lattice would get distorted or locally reduced to stabilize the local excess charge. (3) At the interface, the adsorption of the cation on the terminal group of the oxide could catalyze the interphase transport process by lowering activation energy. In order to further elucidate the cation selectivity of SiO<sub>2</sub>-aqueous system, we investigated transportability of metal ions in SiO<sub>2</sub> structure by ab-initio molecular dynamics (AIMD) simulations and theoretical calculations based on density functional theory (DFT) by assessing the relative stability of metal cations. The mean square displacement of each metal ion calculated by AIMD is depicted in Fig. 5a as a function of simulation time. In order to confirm the smooth movement of ions, we monitored it in the fs time scale at 1800 K. The movement of cations is observed inside SiO<sub>2</sub>. Larger metal ions such as potassium ions can barely migrate in SiO<sub>2</sub> matrix, implying that they are less likely to contribute the breakdown enhancement even if the cations intercalate into the first layer of the matrix. In contrast, the ionic motion of lithium ion is much faster than that of other ions. Drifts of sodium and silver ions are moderately fast. Therefore, we can predict that lithium, sodium and silver ions may affect the breakdown potential once they are transferred from the electrolyte phase. However, the observed  $V_{db}$  shifts cannot be fully addressed, until the solvation energy of each ions are considered. Figure 5b shows the normalized relative stabilities of metal cations in SiO<sub>2</sub> compared to water. We normalized the data using the lowest value, which corresponds to that of sodium ion, for comparison. Positive values for lithium, potassium and cesium ions show that they are not likely to reside in the SiO<sub>2</sub> phase compared with sodium and silver ions. The driving force for the insertion from water to SiO<sub>2</sub> is the highest for sodium and silver ions. Putting together the AIMD simulations and the DFT energy calculations, we can explain why sodium and silver ions modify  $V_{db}$  significantly unlike other alkali metal ions. Computational analysis says that the apparent  $V_{db}$  shift is driven by desolvation energy rather than movement within the SiO<sub>2</sub> phase. Lithium ion has negligible effect on  $V_{db}$  because its insertion from aqueous phase to SiO<sub>2</sub> is energetically unfavorable (Fig. 5b). According to literature, anions can influence the adsorption of alkali metal ions on SiO<sub>2</sub> surface and considerable adsorption of sodium ion is expected when Cl<sup>-</sup> coexists<sup>36</sup>. Reportedly, the partially solvated cation can be adsorbed on the dielectric film and such an intermittent state may affect the cation transfer. Small change in  $V_{db}$  (Fig. S2), however, indicates that this is not the case for this system.

In DFT energy calculation and AIMD simulation, sodium ions and silver ions are almost similar, but as shown in Fig. 3, silver ions have a great effect compared to sodium ions. If the difference between the sodium ion and the silver ion present is that silver ion can be metallization by a weak electric field within the SiO<sub>2</sub><sup>37</sup>. The metallized silver inside the SiO<sub>2</sub> becomes a site for current flow and leads to a breakdown soon, but sodium ions and similar protons do not lead directly to breakdown because they exist only as cations inside SiO<sub>2</sub>.

Neither sodium nor silver effect on breakdown potential is observed at Si<sub>3</sub>N<sub>4</sub> (Fig. 2b), showing that cationic effect is very sensitive to the differences in chemical nature between SiO<sub>2</sub> and Si<sub>3</sub>N<sub>4</sub>. For HfO<sub>2</sub>, silver ion lowers the  $V_{db}$  whereas sodium ion has negligible influence.  $V_{db}$  shift at HfO<sub>2</sub> is observed only for silver ion to 1.2 V, less than for SiO<sub>2</sub>.

AIMD simulations were also performed on Si<sub>3</sub>N<sub>4</sub> and HfO<sub>2</sub> to see transportability of metal ions. AIMD simulations were performed on hexagonal Si<sub>3</sub>N<sub>4</sub> and monoclinic HfO<sub>2</sub> where ion movement was shown only in 1D channel. This 1D channel ion pathway could easily be inhibited due to path-blocking defects<sup>38,39</sup>, unlike 3D

channel of SiO<sub>2</sub>. Since the actual Si<sub>3</sub>N<sub>4</sub> used in the experiments was amorphous possessing numerous defect sites, it is hardly expected that ions drifts in Si<sub>3</sub>N<sub>4</sub> affect the breakdown (Fig. 2b). As for HfO<sub>2</sub>, AIMD simulation shows that all cations do not move, even though strong silver ion induced V<sub>db</sub> lowering was observed in the experiment (Fig. 2c). The difference between the experiment and the simulation could be addressed by the structural variation in the oxides used by each method. The HfO<sub>2</sub> structure we used for AIMD simulation was crystalline HfO<sub>2</sub>, free of structural defects. In the experiment amorphous HfO<sub>2</sub> was used. Unlike the crystalline oxide, amorphous has many different kinds of defects that can allow flow of charge or mass. Silver influence was observed at HfO<sub>2</sub> as well as at SiO<sub>2</sub> while not at Si<sub>3</sub>N<sub>4</sub>, suggesting the role of defects in the ionic conduction in the oxide layers. For HfO<sub>2</sub>, oxygen vacancy is considered a main cause of conduction<sup>40</sup> which could be intrinsically present after the fabrication or possibly be generated under strong electric field. The amorphous HfO<sub>2</sub> film used in the breakdown experiments has a high population of oxygen vacancy due to the stoichiometric imbalance. We assume that these oxygen vacancies may provide a pathway for silver ions movement. In order to find out the relationship between the oxygen vacancy and the conduction of silver ions, oxygen vacancy adjustment was performed. The oxygen vacancies in HfO<sub>2</sub> can be reduced through UV/ozone plasma treatment<sup>41</sup>. The decrease in the population of oxygen vacancies after the treatment was confirmed via X-ray photoelectron spectrum (Fig. S3a). V<sub>db</sub> of HfO<sub>2</sub> was shifted negatively according to UV/ozone plasma treatment by 0.35 V (Fig. S3b), which indicates silver effect on breakdown potential of HfO<sub>2</sub> was weakened with the decrease in oxygen vacancies. The dielectric strength was preserved after the plasma treatment according to the unchanged V<sub>db</sub> in potassium based electrolyte. Given these experimental results, the presence of oxygen vacancies supposedly aids silver ions movement into HfO<sub>2</sub>.

## Conclusions

In this study, we examined the effect of alkali metal and silver ions on the dielectric layer of Si-insulator-electrolyte (EOS) system under the condition of negative electrical bias. Like metal-insulator-electrolyte (MOS) system, the breakdown of insulator in EOS system is observed and its potential, V<sub>db</sub>, depends on the type of dielectric material. V<sub>db</sub> of the Si<sub>3</sub>N<sub>4</sub> remains constant regardless of the monovalent metal ions investigated in this work. On the other hand, the most widely used insulator, SiO<sub>2</sub>, is vulnerable to sodium and silver ions when the solution concentration is higher than 1 mM. HfO<sub>2</sub> film is resistant to sodium ion but significantly influenced by silver ion. The oxygen vacancies of HfO<sub>2</sub> may interact with silver ion. The discriminative influence of cations upon electrical bias in the EOS system was examined in two aspects, molecular dynamics and desolvation of the cations. Lithium, sodium and silver ions clearly show that the breakdown of the dielectric films, V<sub>db</sub>, is driven predominantly by desolvation of ions, which is in contrast to MOS systems.

## Materials and methods

**Materials.** Phosphate buffer solution (PBS) was made using phosphoric acid (Daejung, Korea), potassium phosphate monobasic and potassium phosphate dibasic (99.9%) from Sigma-Aldrich. Highly doped n-type silicon wafer (arsenic-doped, <100>-oriented) with a resistivity as low as 0.005 Ω cm was obtained from STC (Japan). AZ4620 photoresist was purchased from Merck (USA).

**Preparation of thermal oxidized Si/SiO<sub>2</sub>, Si/Si<sub>3</sub>N<sub>4</sub> and Si/HfO<sub>2</sub>.** The 10-nm thick thermal SiO<sub>2</sub> film was prepared by dry oxidation of Si wafer in oxygen environment at 950 °C. Briefly, Si wafer was cleaned with a mixture of H<sub>2</sub>SO<sub>4</sub> and H<sub>2</sub>O<sub>2</sub> before stripping the native oxide by dipping in HF. A 20-nm-thick thermal SiO<sub>2</sub> layer was produced at 850 °C in a furnace with dry O<sub>2</sub> blowing followed by HF wet etching. Repetitive cleaning was followed by dry O<sub>2</sub> blowing in a furnace at 950 °C yielding 10-nm-thick thermal SiO<sub>2</sub> layers. 10-nm-thick Si<sub>3</sub>N<sub>4</sub> was obtained by low pressure chemical vapor deposition (LPCVD) after standard wafer cleaning process. 10-nm HfO<sub>2</sub> layers were deposited by atomic layer deposition (ALD) on same cleaned Si wafer. Tetrakis(ethylmethylamido)hafnium was used as the metal precursor, and deionized H<sub>2</sub>O as the oxygen source. The temperature in the ALD reaction chamber was 200 °C.

**Protective layer coatings on Si/SiO<sub>2</sub>, Si/Si<sub>3</sub>N<sub>4</sub> and Si/HfO<sub>2</sub>.** For reproducible experiments we had to define the exposed SiO<sub>2</sub> area and reduce unwanted pinholes in the oxide film. Successive coatings of alumina, photoresist and photolithography were performed as follows. First of all, 100 nm-thick alumina film was deposited on the whole wafer of Si/SiO<sub>2</sub> by a SNTTEK sputter. AZ4620 photoresist was spin coated on the wafer at 6000 rpm for 30 s and post baking process was conducted at 110 °C for 1.5 min. Then we aligned the wafer under a pattern-designed chromium mask (50 × 50 μm<sup>2</sup>), and exposed it to a UV lamp. Developing was performed by immersing the wafer into AZ300MIF developer (AZ electronic materials) for 2 min. After judging whether the wafer was well developed by optical microscope, a hard bake was performed at 150 °C for 15 min. Etching of alumina was conducted in 50 °C, 85% phosphoric acid for 6 min.

**Electrochemical characterization.** To minimize mechanical stress, we used the whole wafer without a dicing process for all electrochemical experiments<sup>17</sup>. For electrical contact with Si/SiO<sub>2</sub>, Si/Si<sub>3</sub>N<sub>4</sub> and Si/HfO<sub>2</sub>, the insulating layer on the back of silicon wafer was removed by scratching an approximately ~1 cm<sup>2</sup> area with a diamond point pen and casting a droplet of 48% hydrofluoric acid solution<sup>17</sup>. This area was covered by gallium-indium eutectic (≥99.99% trace metals basis from Sigma-Aldrich) then covered by ~10-cm-long conductive adhesive tape<sup>17</sup>. The tape was connected to the working electrode cable of the electrochemical analyzer (CHI660, CH Instrument, US)<sup>17</sup>. 3 μL of 0.5 M aqueous electrolyte was dropped on the exposed SiO<sub>2</sub> area<sup>17</sup>. To complete the electrochemical cell Pt wire and Ag/AgCl reference electrode (3 M KCl) with a double junction filled with 1 M KNO<sub>3</sub> were employed as the counter and reference electrodes, respectively. All potentials in this paper are referenced to Ag/AgCl reference electrode (3 M KCl)<sup>17</sup>. Linear sweep voltammetry (LSV) was carried out to

see characteristic dielectric breakdown behavior of Si/SiO<sub>2</sub>, Si/Si<sub>3</sub>N<sub>4</sub> and Si/HfO<sub>2</sub>. LSV initial potential for SiO<sub>2</sub> and Si<sub>3</sub>N<sub>4</sub> was −3 V, and for HfO<sub>2</sub> was 0 V. The scan rate was 50 mV/s. Potential at which dielectric breakdown occurred ( $V_{db}$ ) was determined as the most positive potential with 100 nA during LSV.

**UV/ozone plasma treatment.** HfO<sub>2</sub> oxidation for eliminating oxygen vacancy was conducted with UV/ozone plasma treatment (AC6, Ahtech LTS, Korea) for 30 min while the distance between the UV lamp and the substrates was maintained at 45 mm.

**Theoretical calculation.** Total energy calculations were performed by using Vienna ab initio Simulation Package (VASP) based on density functional theory<sup>42</sup>. We applied the generalized gradient approximation with the Perdew–Burke–Ernzerhof (PBE) function to treat the exchange–correlation energy<sup>43</sup>. DFT energy calculations were conducted spin-polarized. A kinetic energy cutoff of 600 eV and a  $\Gamma$ -point-only  $k$ -point grid were used, which conditions showed negligible difference with the calculation using a kinetic energy cutoff of 800 eV and a  $2 \times 2 \times 2$   $k$ -point grid based on Monkhorst–Pack scheme<sup>44</sup>. To describe the SiO<sub>2</sub> system, we adopted a  $2 \times 2 \times 2$  supercell of  $\alpha$ -cristobalite structure (space group: P4<sub>1</sub>2<sub>1</sub>2) and let it fully relax until the residual force was less than 0.02 eV/Å. We estimated the relative stability of various alkali metal ions in between two mediums. One is in the solution, and the other is in interstitial sites in SiO<sub>2</sub>. The relative stability,  $\Delta E$ , can be expressed as:

$$\Delta E(x) = E_{x \text{ in SiO}_2}(x) - E_{\text{SiO}_2} - \{E_{x \text{ in vacuum}}(x) + E_{\text{solvation}}(x)\}$$

where  $x$  is alkali metal ion such as Li<sup>+</sup>, Na<sup>+</sup>, K<sup>+</sup>, Rb<sup>+</sup>, Cs<sup>+</sup> and Ag<sup>+</sup>. To determine the most stable interstitial sites in SiO<sub>2</sub>, we considered seven different interstitial sites generated from Voronoi analysis<sup>45</sup>. Subsequently, the lowest-DFT-energy structure was selected to estimate  $E_{x \text{ in SiO}_2}(x)$  that contains one alkali metal ion. Only the internal atomic positions were allowed relax while the lattice constants were fixed to those of the fully-relaxed SiO<sub>2</sub> structure when we calculate  $E_{x \text{ in SiO}_2}(x)$ .  $E_{\text{SiO}_2}$  is the DFT energy of  $2 \times 2 \times 2$  supercell of  $\alpha$ -cristobalite structure. Energy of single alkali metal ion in the vacuum,  $E_{x \text{ in vacuum}}(x)$ , was obtained from a  $20 \times 20 \times 20$  Å<sup>3</sup> cubic cell with one ion in the box. The energy of the single ion was corrected by using solvation energy,  $E_{\text{solvation}}(x)$ , to estimate the energy of ion in solvated states (Table S1). Ab initio molecular dynamics simulations were carried out by employing VASP based on Verlet algorithm<sup>46</sup>. The same structures which were used for calculating  $E_{x \text{ in SiO}_2}(x)$  were adopted for AIMD simulations except for the Cs<sup>+</sup>-inserted SiO<sub>2</sub> case where the electronic energy could not be converged in AIMD calculation conditions. We also did AIMD simulations on hexagonal Si<sub>3</sub>N<sub>4</sub> (space group: P6<sub>3</sub>/m) and monoclinic HfO<sub>2</sub> (space group: P2<sub>1</sub>/c) using a  $\Gamma$ -point-only  $k$ -point grid and a cutoff energy of 400 eV. The simulations were performed for 200 ps after an equilibrium step of 10 ps in the canonical (NVT) ensemble with a Nosé–Hoover thermostat<sup>47,48</sup>. All AIMD simulations were conducted at an elevated temperature of 1800 K to facilitate the ionic motions.

Received: 7 May 2020; Accepted: 17 July 2020

Published online: 08 October 2020

## References

- Liu, Z. *et al.* Silicon oxides: a promising family of anode materials for lithium-ion batteries. *Chem. Soc. Rev.* **48**, 285–309 (2019).
- Jung, S. C. & Han, Y. K. How do Li atoms pass through the Al<sub>2</sub>O<sub>3</sub> coating layer during lithiation in Li-ion batteries?. *J. Phys. Chem. Lett.* **4**, 2681–2685 (2013).
- Jung, S. C., Kim, H. J., Choi, J. W. & Han, Y. K. Sodium ion diffusion in Al<sub>2</sub>O<sub>3</sub>: A distinct perspective compared with lithium ion diffusion. *Nano Lett.* **14**, 6559–6563 (2014).
- Lee, J. Y. *et al.* Hydrogen-atom-mediated electrochemistry. *Nat. Commun.* **4**, 1–8 (2013).
- Esposito, D. V., Levin, I., Moffat, T. P. & Talin, A. A. H<sub>2</sub> evolution at Si-based metal–insulator–semiconductor photoelectrodes enhanced by inversion channel charge collection and H spillover. *Nat. Mater.* **12**, 562–568 (2013).
- Ji, L. *et al.* Localized dielectric breakdown and antireflection coating in metal–oxide–semiconductor photoelectrodes. *Nat. Mater.* **16**, 127–131 (2016).
- Leighton, C. Electrolyte-based ionic control of functional oxides. *Nat. Mater.* **18**, 13–18 (2019).
- Chun, H. & Chung, T. D. Iontronics. *Annu. Rev. Anal. Chem.* **8**, 441–462 (2015).
- Chen, Y. W. *et al.* Atomic layer-deposited tunnel oxide stabilizes silicon photoanodes for water oxidation. *Nat. Mater.* **10**, 539–544 (2011).
- Velmurugan, J., Zhan, D. & Mirkin, M. V. Electrochemistry through glass. *Nat. Chem.* **2**, 498–502 (2010).
- Esposito, D. V., Levin, I., Moffat, T. P. & Talin, A. A. H<sub>2</sub> evolution at Si-based metal–insulator–semiconductor photoelectrodes enhanced by inversion channel charge collection and H spillover. *Nat. Mater.* **12**, 562–568 (2013).
- Kwok, H., Briggs, K. & Tabard-Cossa, V. Nanopore fabrication by controlled dielectric breakdown. *PLoS ONE* **9**, e92880 (2014).
- Briggs, K. *et al.* Kinetics of nanopore fabrication during controlled breakdown of dielectric membranes in solution. *Nanotechnology* **26**, 084004 (2015).
- Wang, Y., Chen, Q., Deng, T. & Liu, Z. Nanopore fabricated in pyramidal HfO<sub>2</sub> film by dielectric breakdown method. *Appl. Phys. Lett.* **111**, 143103 (2017).
- Mibus, M. *et al.* Dielectric breakdown and failure of anodic aluminum oxide films for electrowetting systems. *J. Appl. Phys.* **114**, 014901 (2013).
- Liu, Y. *et al.* In situ transmission electron microscopy observation of pulverization of aluminum nanowires and evolution of the thin surface Al<sub>2</sub>O<sub>3</sub> layers during lithiation–delithiation cycles. *Nano Lett.* **11**, 4188–4194 (2011).
- Yun, J. *et al.* Dielectric breakdown and post-breakdown dissolution of Si/SiO<sub>2</sub> cathodes in acidic aqueous electrochemical environment. *Sci. Rep.* **8**, 1–7 (2018).
- Lee, J. G. *et al.* Conduction through a SiO<sub>2</sub> layer studied by electrochemical impedance analysis. *Electrochem. Commun.* **76**, 75–78 (2017).
- Lombardo, S. *et al.* Dielectric breakdown mechanisms in gate oxides. *J. Appl. Phys.* **98**, 12 (2005).

20. Osburn, C. M. & Ormond, D. W. Sodium-induced barrier-height lowering and dielectric breakdown on SiO<sub>2</sub> films on silicon. *J. Electrochem. Soc.* **121**, 1195 (1974).
21. Cui, H. & Burke, P. A. Time-dependent dielectric breakdown studies of PECVD H:SiCN and H:SiC thin films for copper metalization. *J. Electrochem. Soc.* **151**, G795 (2004).
22. Derbenwick, G. F. Mobile ions in SiO<sub>2</sub>: potassium. *J. Appl. Phys.* **48**, 1127–1130 (1977).
23. Bonilla, R. S. & Wilshaw, P. R. Potassium ions in SiO<sub>2</sub>: electrets for silicon surface passivation. *J. Phys. D Appl. Phys.* **51**, 25101 (2018).
24. Sivonxay, E., Aykol, M. & Persson, K. A. The lithiation process and Li diffusion in amorphous SiO<sub>2</sub> and Si from first-principles. *Electrochim. Acta* **331**, 135344 (2020).
25. Bonilla, R. S. & Wilshaw, P. R. Potassium ions in SiO<sub>2</sub>: electrets for silicon surface passivation. *J. Phys. D Appl. Phys.* **51**, 025101 (2018).
26. Stagg, J. P. Drift mobilities of Na<sup>+</sup> and K<sup>+</sup> ions in SiO<sub>2</sub> films. *Appl. Phys. Lett.* **31**, 532–533 (1977).
27. Fishbein, B. J. & Plummer, J. D. Characterization of cesium diffusion in silicon dioxide films using backscattering spectrometry. *Appl. Phys. Lett.* **50**, 1200–1202 (1987).
28. Vakula, N. I., Kuramshina, G. M., Gorb, L. G., Hill, F. & Leszczynski, J. Adsorption and diffusion of a silver atom and its cation on α-SiO<sub>2</sub> (0 0 1): comparison of a pure surface with a surface containing an Al defect. *Chem. Phys. Lett.* **567**, 27–33 (2013).
29. Burgess, T. E., Baum, J. C., Fowkes, F. M., Holmstrom, R. & Shirn, G. A. Thermal diffusion of sodium in silicon nitride shielded silicon oxide films. *J. Electrochem. Soc.* **116**, 1005 (1969).
30. Bolland, B. Thermally stimulated current properties of alkaline ions in CVD Si<sub>3</sub>N<sub>4</sub>. *J. Electrochem. Soc.* **137**, 2845 (1990).
31. Cook, T. E. *et al.* Band offset measurements of the Si<sub>3</sub>N<sub>4</sub>/GaN (0001) interface. *J. Appl. Phys.* **94**, 3949–3954 (2003).
32. Bersch, E., Rangan, S., Bartynski, R. A., Garfunkel, E. & Vescovo, E. Band offsets of ultrathin high-κ oxide films with Si. *Phys. Rev. B Condens. Matter Mater. Phys.* **78**, 1–10 (2008).
33. Pan, P. Effects of processing on characteristics of 10–15 nm thermally grown SiO<sub>2</sub> films. *J. Electrochem. Soc.* **133**, 1171 (1986).
34. Yota, J., Shen, H. & Ramanathan, R. Characterization of atomic layer deposition HfO<sub>2</sub> Al<sub>2</sub>O<sub>3</sub> and plasma-enhanced chemical vapor deposition Si<sub>3</sub>N<sub>4</sub> as metal–insulator–metal capacitor dielectric for technology. *J. Vac. Sci. Technol. A Vac. Surf. Film* **31**, 01A134 (2013).
35. Takagi, K. & Ono, T. First-principles study on leakage current caused by oxygen vacancies at HfO<sub>2</sub>/SiO<sub>2</sub>/Si interface. *Jpn. J. Appl. Phys.* **57**, 066501 (2018).
36. Pfeiffer-Laplaud, M. & Gaigeot, M. P. Electrolytes at the hydroxylated (0001) α-quartz/water interface: location and structural effects on interfacial silanols by DFT-based MD. *J. Phys. Chem. C* **120**, 14034–14047 (2016).
37. Tian, X. *et al.* Bipolar electrochemical mechanism for mass transfer in nanoionic resistive memories. *Adv. Mater.* **26**, 3649–3654 (2014).
38. Malik, R., Burch, D., Bazant, M. & Ceder, G. Particle size dependence of the ionic diffusivity. *Nano Lett.* **10**, 4123–4127 (2010).
39. Chung, S. Y., Choi, S. Y., Yamamoto, T. & Ikuhara, Y. Atomic-scale visualization of antisite defects in LiFePO<sub>4</sub>. *Phys. Rev. Lett.* **100**, 1–4 (2008).
40. Sun, C. *et al.* The resistive switching characteristics of TiN/HfO<sub>2</sub>/Ag RRAM devices with bidirectional current compliance. *J. Electron. Mater.* **48**, 2992–2999 (2019).
41. Kumar, M., Jeong, H. & Lee, D. Effect of UV/ozone plasma treatment on sol–gel-derived HfO<sub>2</sub> thin films. *Ceram. Int.* **43**, 1174–1179 (2017).
42. Kresse, G. & Furthmüller, J. Efficient iterative schemes for ab initio total-energy calculations using a plane-wave basis set. *Phys. Rev. B Condens. Matter Mater. Phys.* **54**, 11169–11186 (1996).
43. Perdew, J. P., Burke, K. & Ernzerhof, M. The stability of ionic crystal surfaces. *J. Phys. C Solid State Phys.* **12**(22), 4977 (1996).
44. Chadi, D. J. Special points for Brillouin-zone integrations. *Phys. Rev. B* **16**, 1746–1747 (1977).
45. Ong, S. P. *et al.* Python materials genomics (pymatgen): a robust, open-source python library for materials analysis. *Comput. Mater. Sci.* **68**, 314–319 (2013).
46. Verlet, L. Computer, “experiments” on classical fluids. I. Thermodynamical properties of Lennard–Jones molecules. *Phys. Rev.* **159**, 183–195 (1967).
47. Nosé, S. A unified formulation of the constant temperature molecular dynamics methods. *J. Chem. Phys.* **81**, 511–519 (1984).
48. Hoover, W. G. Hoover WG (1985) Canonical dynamics: equilibrium phase-space distributions. *Phys. Rev. A* **31**, 1695–1697. <https://doi.org/10.1103/PhysRevA.31.1695> (1985).

## Acknowledgements

This research was supported by the National Research Foundation of Korea (NRF) Grant funded by the Korean Government (MSIT) (No. 2017R1E1A1A01074236).

## Author contributions

J.Y. and J.G.L. designed and performed all experiments, and they contributed equally to this work, J.G.L. conducted the electrochemical experiments, K.O. and K.K. performed and interpreted the computational results, T.D.C. supervised the overall project.

## Competing interests

The authors declare no competing interests.

## Additional information

**Supplementary information** is available for this paper at <https://doi.org/10.1038/s41598-020-73880-w>.

**Correspondence** and requests for materials should be addressed to T.D.C.

**Reprints and permissions information** is available at [www.nature.com/reprints](http://www.nature.com/reprints).

**Publisher's note** Springer Nature remains neutral with regard to jurisdictional claims in published maps and institutional affiliations.



**Open Access** This article is licensed under a Creative Commons Attribution 4.0 International License, which permits use, sharing, adaptation, distribution and reproduction in any medium or format, as long as you give appropriate credit to the original author(s) and the source, provide a link to the Creative Commons licence, and indicate if changes were made. The images or other third party material in this article are included in the article's Creative Commons licence, unless indicated otherwise in a credit line to the material. If material is not included in the article's Creative Commons licence and your intended use is not permitted by statutory regulation or exceeds the permitted use, you will need to obtain permission directly from the copyright holder. To view a copy of this licence, visit <http://creativecommons.org/licenses/by/4.0/>.

© The Author(s) 2020